Available online at www.sciencedirect.com

SCIENCE DIRECT®

Tectonophysics 406 (2005) 213–231

TECTONOPHYSICS

www.elsevier.com/locate/tecto

Anomalous lithospheric structure of Northern Juan de Fuca plate — a consequence of oceanic rift propagation?

Alastair F. McClymont*, Ron M. Clowes

Department of Earth and Ocean Sciences, University of British Columbia, 6339 Stores Road, Vancouver, BC, Canada V6T 1Z4

Received 29 June 2004; received in revised form 13 May 2005; accepted 17 May 2005

Abstract

Anomalous crustal and upper mantle structure of northern Juan de Fuca plate is revealed from wide-angle seismic and gravity modelling. A 2-D velocity model is produced for refraction line II of the 1980 Vancouver Island Seismic Project (VISP80). The refraction data were recorded on three ocean bottom seismometers (OBSs) deployed at the ends and middle of a 110 km line oriented parallel to the North American continental margin. The velocity model is constructed via ray tracing and conforms to first-arrival amplitude observations and travel time picks of direct, converted and reflected phases. Between sub-sediment depths of ~3 to ~11 km, depths normally associated with the lower crust and upper oceanic mantle, the final model shows that compressional-wave velocities decrease significantly from southeast to northwest along the profile. At sub-sediment depths of ~11 km at the northwestern end of the profile, P-wave velocities are as low as 7.2 km/s. A complementary 2-D gravity model using the geometry of the velocity model and velocity–density relationships characteristic of oceanic crust is produced. The high densities required to match the gravity field indicate the presence of peridotites containing 25–30% serpentine by volume, rather than excess gabbroic crust, within the deep low velocity zone. Anomalous travel time delays and unusual reflection characteristics observed from proximal seismic refraction and reflection experiments suggest a broader zone of partially serpentinized peridotites coincident with the trace of a pseudofault. We propose that partial serpentinization of the upper mantle is a consequence of slow spreading at the tip of a propagating rift.

Keywords: Juan de Fuca plate; Crustal structure; Serpentinized peridotites; Pseudofault; Seismic refraction; Gravity modelling

1. Introduction

Normal oceanic crust has a characteristic structure and composition (White et al., 1992; Christensen, 1978). From an extensive compilation of marine seismic refraction surveys within the Pacific and Atlantic Ocean basins, White et al. (1992) report a mean thick-

* Corresponding author. Present address. Institute of Geophysics, ETH-Hoenggerberg, CH-8093, Zurich, Switzerland. Tel.: +41 1 6332727; fax: +41 1 6331065.

E-mail address: amcclymont@aug.ig.erdw.ethz.ch (A.F. McClymont).

0040-1951/$ - see front matter © 2005 Elsevier B.V. All rights reserved.
doi:10.1016/j.tecto.2005.05.026

ness of 7.1 ± 0.8 km for the igneous section of oceanic crust. Variations from the normal model of oceanic crust are known to occur at anomalous geological settings, including fracture zones along the slow spreading Mid-Atlantic Ridge where seismic studies indicate unusually thin crust and low compressional wave velocities between offset spreading ridge segments (Detrick et al., 1993). The formation of thin crust at ridge-transform intersections is attributed to decreased melt supply at the ends of the spreading ridge segments in response to their juxtaposition against a cold lithospheric edge (Fox and Gallo, 1984).

Pseudofaults are analogous to fracture zones because they also represent a boundary between litho-

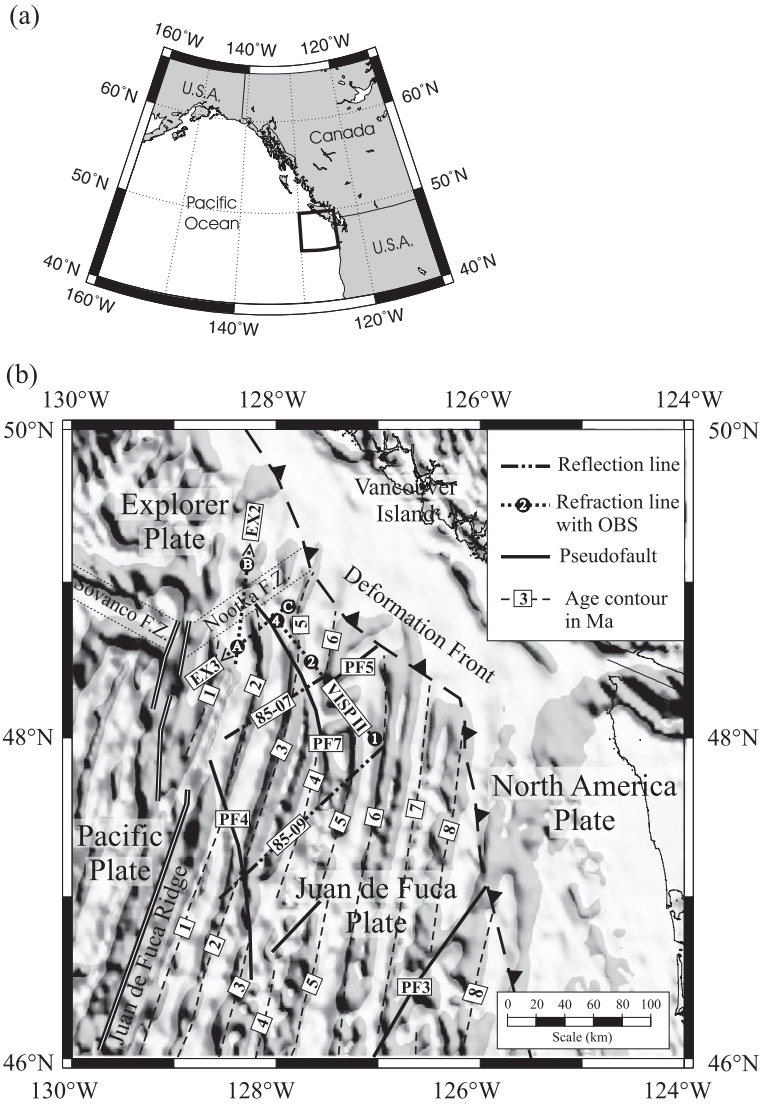

Fig. 1. (a) Location map for Fig. 1b. (b) Shaded relief map of magnetic anomalies over northern Juan de Fuca plate. Positive anomalies are shown with a grey fill. Magnetic data are from the National Geophysical Data Center (http://www.ngdc.noaa.gov) maintained by the National Oceanic and Atmospheric Administration. Included are age contours, pseudofault locations (from Wilson (1993)), major fault/fracture zones (F.Z.) and the location of seismic refraction and reflection lines VISP II (this study), EX2, EX3 (Au and Clowes, 1982), 85-07 and 85-09 (Hasselgren and Clowes, 1995). VISP II OBSs are designated numbers (1, 2 and 4) while OBSs for lines EX2 and EX3 are indicated by letter (A, B and C); arrowheads on lines EX2 and EX3 indicate the forward shooting direction.

sphere of contrasting age. At a propagating rift tip, crustal accretion is perturbed by the cold lithosphere into which the rift is extending and a "wake" of slow spreading crust should be preserved along the trailing pseudofaults (Kleinrock and Hey, 1989). Kruse et al. (2000) show similarities between gravity anomalies over Atlantic fracture zones and those over the Mathematician, Bauer, Easter, Juan Fernandez and Northern Chile Ridge pseudofaults. Mantle Bouguer anomalies over the outer pseudofault of the Juan Fernandez microplate are 5–15 mGal highs that correlate with thin and possibly denser than average oceanic crust (Kruse et al., 2000).

In the northeastern Pacific Ocean (Fig. 1a), the Juan de Fuca ridge system that lies offshore of western North America has undergone 20° of clockwise rotation since 9 Ma (Davis and Currie, 1993). The disrupted pattern of magnetic anomalies on the adjacent Pacific and Juan de Fuca plates is consistent with a series of ridge propagation events (Wilson et al., 1984). From two multichannel seismic reflection lines (85-07 and 85-09, Fig. 1b), Hasselgren et al. (1992) interpret two zones of crustal underplating within the Juan de Fuca plate coincident with two outer pseudofaults. The results of their study have not been reconciled with the gravity field over the Juan de Fuca plate.

We present the results of a wide-angle seismic line within the vicinity of pseudofault 7 (PF7) on the northern Juan de Fuca plate (Fig. 1b). A 2-D model of the velocity structure and a complementary 2-D gravity model are used to interpret lithospheric structure. Our interpretation is related to results from proximal seismic lines to consider the influence of propagation rifting on the crustal and upper mantle structure of northern Juan de Fuca plate.

2. Seismic data

The marine seismic refraction data (line VISP II in Fig. 1b) were acquired as one component of the 1980 Vancouver Island Seismic Project (VISP 80) described in full by Ellis et al. (1983). Three ocean bottom seismometers (OBSs), which recorded explosive and airgun shots, were deployed at the ends and middle of a 110 km line oriented parallel to the Cascadia deformation front, located about 40–50 km to the northeast, on the Juan de Fuca plate. The structure of the basement topography and the division between two layers of hemipelagic and turbiditic sediments over the length of the profile is provided from an interpretation of additional single channel continuous seismic profiling (CSP) data (H. White and R. Clowes, unpublished study).

The OBSs recorded signals from one vertical and two horizontal geophones plus one hydrophone on analogue magnetic tape. The airgun source was a single 32 l (2000 cu in) Bolt airgun fired at 13.8 MPa at nominal intervals of 0.5 km. Explosive sources ranged in size from 500 to 25 kg of marine seismic explosives. Large charges ranging from 500 (at the ends of the line) to 100 kg were detonated at 10 or 7.5 km intervals. In between these larger charges, at nominal intervals of 2.5 km, charges of 25 or 50 kg were detonated. Amplitudes were corrected for charge sizes using standard procedures (e.g., O'Brien, 1960; Mueller et al., 1962). The analogue magnetic tapes were converted to digital tape format following completion of the experiment. However, the data tapes have subsequently disappeared or been rendered unreadable. A selection of the original receiver gathers (Table 1) are available in hardcopy format plotted with a reduction velocity of 6 km/s. These gathers were digitised by a commercial company that specializes in recovery of seismic data from paper records.

The airgun source data for OBS-2 exhibit a variety of direct, converted and multiply reflected phases (Fig. 2). These include PPS, a secondary phase that is attributed to a P- to S-wave conversion of the ascending rays at the sediment/basement interface beneath each OBS and is also evident on horizontal

Table 1
Data coverage recovered from digitized paper records for line VISP II

Receiver and component	Source and offset range	
	Explosive	Airgun
OBS-1: vertical	5 to 110 km	
OBS-1: horizontal	5 to 80 km	
OBS-2: vertical	−75 to 40 km	−30 to 30 km
OBS-2: horizontal	−75 to 40 km	−30 to 30 km
OBS-4: vertical	−15 to −115 km	
OBS-4: hydrophone	−15 to −75 km	

Explosive source shots were fired with a spacing of ~2.5 km and airgun shots were fired with a spacing of ~0.5 km.

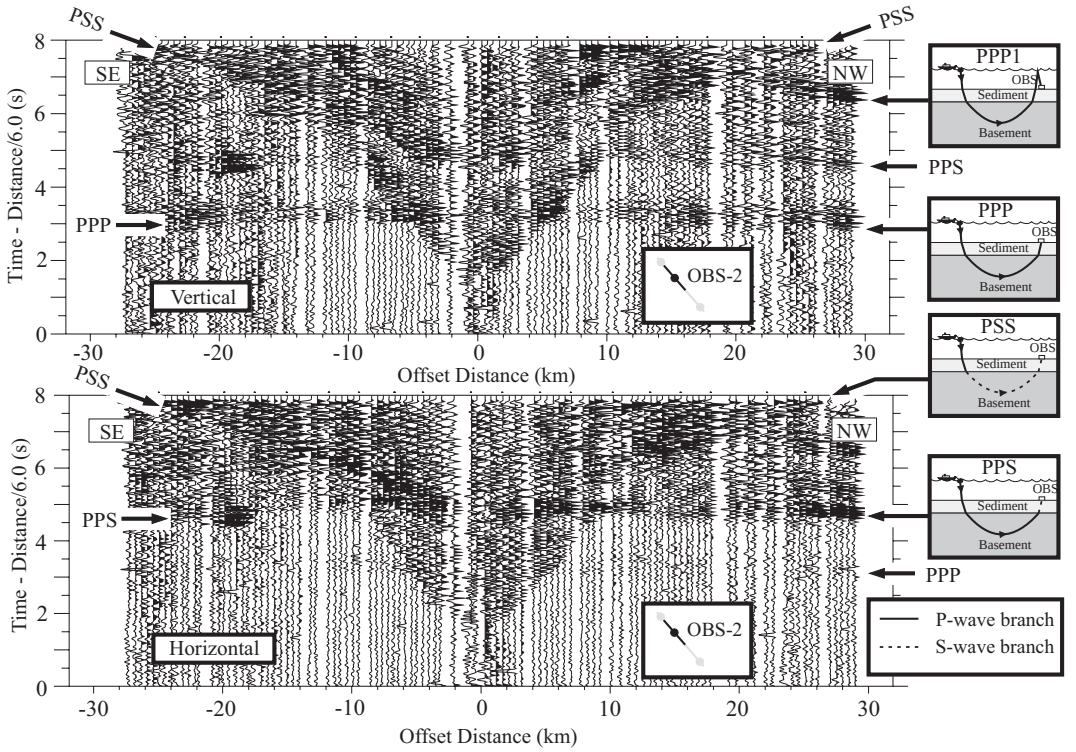

Fig. 2. Vertical and horizontal component receiver gathers for OBS-2 from the airgun source. On this and similar Figures, the inset box placed on top of the receiver gathers shows the featured OBS location (black circle) and line coverage (black) relative to the rest of the line and other OBSs (shaded grey). The box diagrams to the right illustrate the interpreted geometry and terminology of all the converted and reflected raypath phases observed from the data; arrows identify the phases. The PPP phase classification encompasses both Pc and Pn.

and vertical component gathers of the longer offset, explosive source data (e.g. OBS-2, Fig. 3). The PPS phase arrives with a near uniform time delay after the first turning ray arrivals that varies slightly with the thickness of the sediments beneath each OBS (~2 s). The transition from the crustal turning ray phase (Pc) to the mantle turning ray phase (Pn) arrivals is interpreted from the abrupt decrease in amplitude size and from the onset of phase velocities greater than 7.6 km/s (Fig. 3).

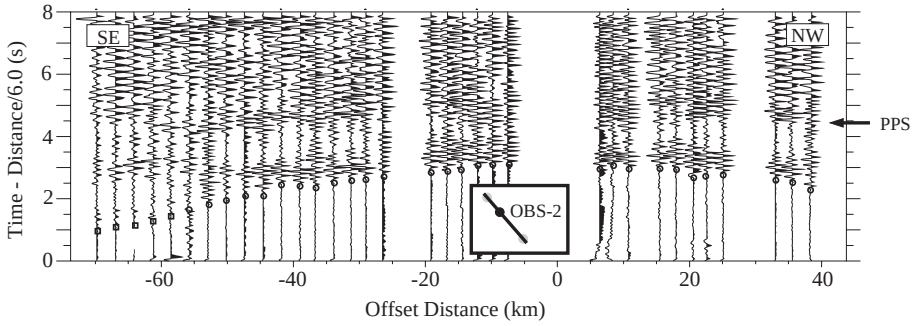

Fig. 3. Vertical component receiver gather for OBS-2 from the explosive source. Circles indicate crustal turning ray phase picks (Pc), squares are mantle turning ray phase picks (Pn). The PPS phase is more prominent on the horizontal component but is discernible on the vertical component.

Forward and reverse, explosive source, vertical component receiver gathers from the OBSs at the ends of line VISP II (OBS-1 and OBS-4, Figs. 4a and 5b) indicate laterally variable velocity structure in the deep crust and upper mantle. Turning ray first arrival phases are discernible out to at least 60 km

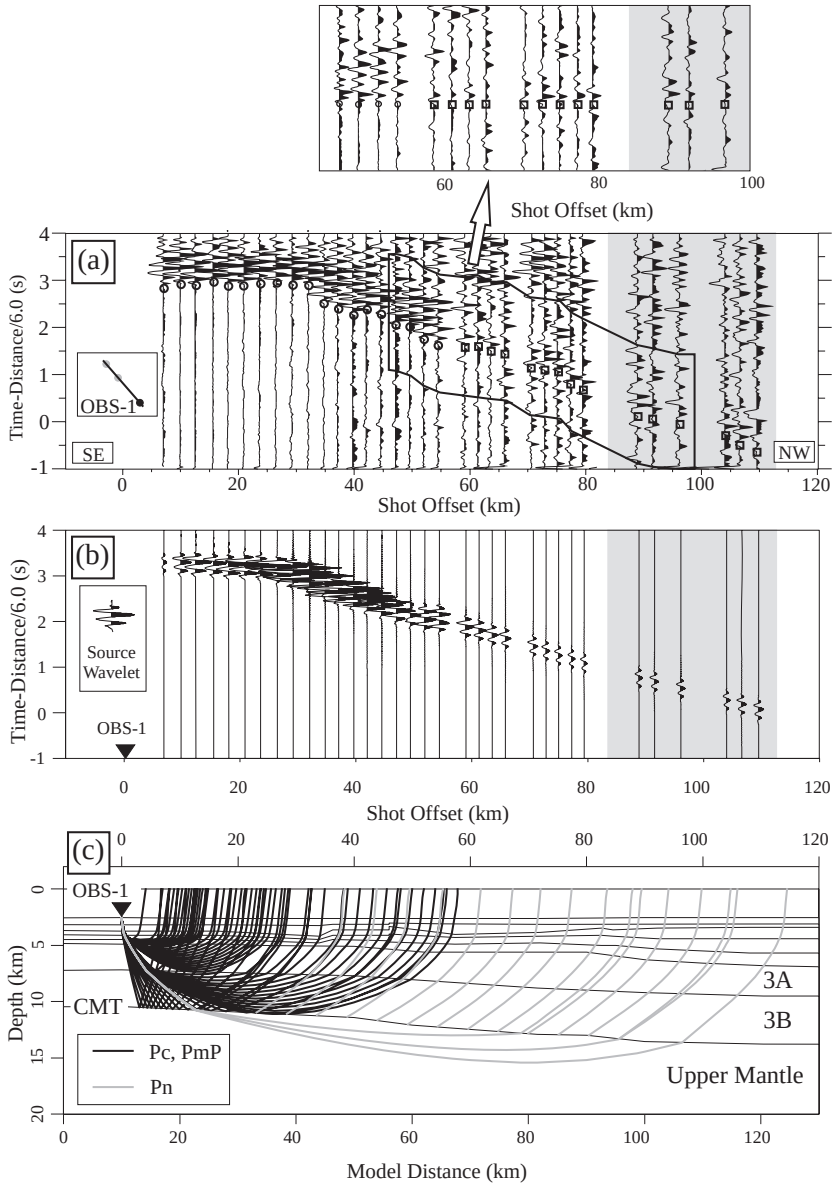

Fig. 4. Observed and calculated data for OBS-1, explosive source, vertical component. (a) First arrival Pc (circles) and Pn (squares) picks from the observed receiver gather. Amplitudes are scaled with an r correction factor to enhance the signal with shot offset. Data from the window outlined between 45 and 100 km offset are shown above where each trace is levelled to the first arrival pick datum to illustrate trace-to-trace correlations of the proceeding waveforms. Picks made from traces with a shot offset of greater than 80 km (displayed on grey background) are considered poor due to low S/N. (b) Synthetic first arrival data generated from the final model (Fig. 7) for which the layer outline is shown in (c). The source wavelet is plotted to the same scale as the travel time axis. Amplitudes are scaled as in (a). (c) Ray coverage of the velocity model. Seismic layers 3A, 3B and the upper mantle and the crust–mantle transition (CMT) are labelled.

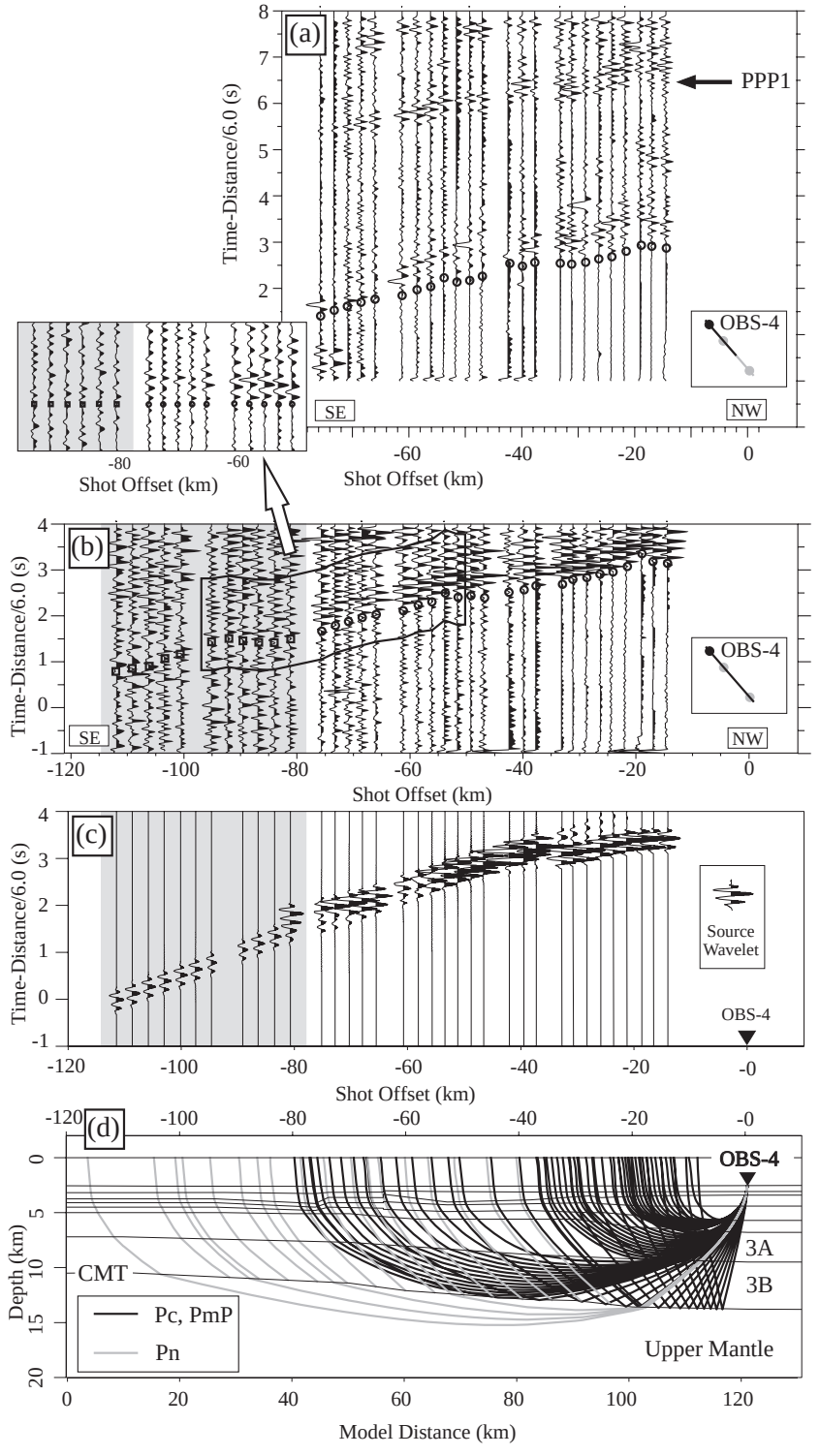
(a)
PPP1
Time-Distance/6.0 (s)
OBS-4
SE
NW
Shot Offset (km)
(b)
Time-Distance/6.0 (s)
OBS-4
SE
NW
Shot Offset (km)
(c)
Time-Distance/6.0 (s)
Source Wavelet
OBS-4
Shot Offset (km)
(d)
Depth (km)
OBS-4
3A
3B
CMT
Pc, PmP
Pn
Upper Mantle
Model Distance (km)

Table 2
Pick uncertainties for all phases observed from the seismic data

Phase	n	Uncertainty range (s)	Median uncertainty (s)
Pc	155	0.025–0.150	0.05
Pn	36	0.100–0.440	0.15
PPS	138	0.035–0.150	0.10
PSS	56	0.035–0.150	0.15
PPP1	46	0.035–0.150	0.15

Parameter n is the number of picks for each phase group.

shot offset on OBS-1 and to 80 km offset on OBS-4. Some picks were made on consecutive traces by correlating waveforms where it became difficult to distinguish the first recorded signal from background noise (Figs. 4a, 5b).

3. Velocity model

A 2-D velocity model is constructed using various applications of the RAYINVR ray tracing algorithm (Zelt and Smith, 1992). Phase travel times picked from the seismic data are used as input. Uncertainties for each pick are assigned on the basis of the signal-to-noise ratio (S/N) within a time window before and after each pick (Table 2).

An initial 1-D velocity model was constructed to approximately match calculated and observed travel times. The model consists of 9 layers with vertical velocity gradients: 1 layer to represent seawater, 2 layers for the marine sediments, 5 layers for the igneous section of oceanic crust (seismic layers 2A, 2B, 2C, 3A and 3B after Ewing and Houtz (1979)) and 1 layer for the upper mantle. Within RAYINVR, each layer is described in 2-D model space with boundary nodes that represent a position (x, z) and a velocity (v). Rays were traced through the initial model and layer boundary structure was manually modified to improve the fit of the travel time residuals. The boundaries of the layers within the crust represent changes in velocity gradient rather than sharp changes in velocity.

Modifications to the 2-D model were designed to improve the fit of the travel time residuals with the minimum possible deviation from the normal thickness of oceanic crust (~7 km (White et al., 1992)). Velocity nodes at layer boundaries were subsequently edited to incorporate lateral variability of velocities within each layer, improve the travel time residuals and avoid creating complicated layer structure. Finally, the RAYINVR inversion routine (Zelt and Smith, 1992) was applied to fine tune the fit of calculated travel times to observed travel times by updating the model velocity nodes without introducing anomalous velocity structure.

Improvements to the velocity model were evaluated at each modelling step using root-mean-square (T_{RMS}) and normalized chi squared (χ^2) statistical tests of the travel time residuals (Table 3). To achieve an optimal fit to the data, the maximum number of rays should be traced to their observation points and the χ^2 value should be minimized to as close to one as possible. The VISP II travel time observations are irregularly spaced such that some regions beneath the profile are better sampled than others. Following the strategy described by Zelt (1999), we present a final model that is relatively coarsely parameterized and accept a χ^2 value greater than one. Layer parameters for the final velocity model are listed in Table 4.

Converted and reflected phases picked from the observed data are included to further test the 2-D model (e.g., Fig. 2). Turning ray phases modified to incorporate phase conversions at the sediment/basement interface and reflections at the free water surface are traced through the model to simulate PPS, PSS and PPP1. A uniform P- to S-wave velocity conversion is applied to each layer using an assigned Poisson's ratio (σ). Poisson's ratio is adjusted for each layer to best fit the data picks for converted phases PPS and PSS. Fig. 6 displays the calculated travel times for the primary, converted and water multiple phases relative to picks made from the OBS-2, airgun source receiver gathers shown in

Fig. 5. Observed and calculated data for OBS-4, explosive source. (a) First arrival picks from the observed hydrophone receiver gather. Amplitudes are scaled with an r correction factor. (b) First arrival picks from the observed vertical component receiver gather. Amplitudes are scaled as in (a). Data from the window outlined between −50 km and −95 km offset are shown above with each trace levelled to the first arrival pick datum. (c) Synthetic first arrival data generated from the final model (Fig. 7) for which the layer outline is shown in (d). Amplitudes are scaled as in (a). (d) Ray coverage of the velocity model.

Table 3
T_{RMS} and χ^2 of first arrival residual travel times evaluated at each model step

Model step	0 to 80 km			0 to 120 km		
	T_{RMS} (s)	χ^2	n	T_{RMS} (s)	χ^2	n
1) Initial 1-D model	0.154	5.887	139	0.223	5.432	161
2) 2-D forward model	0.087	1.808	164	0.145	1.804	189
3) 2-D model after inversion	0.083	1.573	167	0.137	1.604	189

Statistics are shown for the travel time data with (191 picks) and without (169 picks) the low quality data (greater than 80 km offset in Figs. 4 and 5).

Fig. 2. The observed converted phases are relatively well fit by data generated from the model and indicate that, beneath OBS-2, S-wave velocity structure and Poisson's ratios for seismic layers 1A to 2C (see Table 4) are consistent with highly water saturated marine sediments and igneous basalts (Christensen, 1996).

Observed travel times and travel times calculated from the best fit velocity model for the explosive source data are shown in Fig. 7a. The final model (Fig. 7b) represents a good fit to the explosive data for all 3 OBSs out to 80 km shot offset. For explosive source picks from offsets greater than 80 km, the optimal model solution is a compromise yielding calculated travel times too early for OBS-2 and OBS-4 and too late for OBS-1 picks.

Table 4
Vertical layer thickness (ΔZ), P-wave (α) and S-wave (β) velocities, Poisson's ratio (σ) and Q_p parameters for the final velocity model

Layer	ΔZ (km)	α (km/s)	β (km/s)	σ	Q_p
Sea water	2.53–2.60	1.49	–	0.50	1000[a]
Sediments (1A)	0.41–0.63	1.73–1.90	0.47–0.52	0.46	10[a]
Sediments (1B)	0.36–0.91	2.28–2.39	0.69–0.72	0.45	10[a]
2A	0.27–0.99	3.46–4.54	1.85–2.43	0.30	25[b]
2B	0.30–1.30	4.96–5.93	2.86–3.42	0.25	150[b]
2C	0.25–1.10	5.94–6.33	3.43–3.65	0.25	450[c]
3A	2.30–3.20	6.19–7.02	–	–	450[c]
3B	3.30–4.30	7.04–7.80	–	–	450[c]
Upper mantle	–	7.72–8.20	–	–	450[c]

These are the range of values for each parameter including the lateral variations within the model. Hence parameter values for one layer can overlap with those of another. Parameters β and σ for seismic layers 2A, 2B and 2C are based on limited observations of the PSS phase from the airgun data (Fig. 2). Parameter Q_p values are assumed from other studies: (a) are from Best et al. (2001), (b) are from Jacobson and Lewis (1990) and (c) are from Spudich and Orcutt (1980).

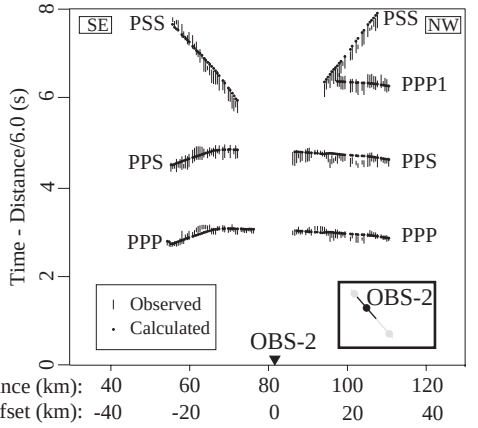

Fig. 6. Observed primary and secondary arrivals from OBS-2 airgun source record sections (Fig. 2) and those calculated from the 2-D model. Each observed pick is plotted as a vertical bar for which the length defines the uncertainty.

For an additional check of the validity of the 2-D model, synthetic receiver gather seismograms are produced from the model for comparison with the recorded data (Figs. 4, 5). Amplitudes of the turning ray phases and a reflection phase from the Moho (PmP) are calculated by RAYINVR using zero-order asymptotic ray theory (Zelt and Ellis, 1988). A compressional wave quality factor (Q_p) is assigned to each layer of the model to account for energy loss by anelastic attenuation (Table 4). The source wavelet is produced from stacked first arrivals of the observed data. The relative amplitudes of the first arrival synthetic data appear to mimic those for the sections recorded on the vertical component of OBS-1 and OBS-4 from the explosive source (Figs. 4a,b, 5b,c). OBS-1 synthetic data exhibit a pattern of relatively large amplitudes out to 56 km shot offset followed by an abrupt change to relatively low amplitudes. The transition to low amplitudes at ~60 km shot offset is coincident with that shown by the recorded data (Fig. 4a) and indicates a relatively low velocity gradient at a depth of ~10 km as would be expected at depths normally associated with the upper mantle. The same change, from high amplitudes to low amplitudes, is apparent from OBS-4 synthetic data at ~80 km shot offset. It is difficult to locate this feature with the same accuracy in the recorded data as it is masked by significant noise. Large amplitudes are coherent to at least 70 km offset suggesting that a layer of low velocity gradient

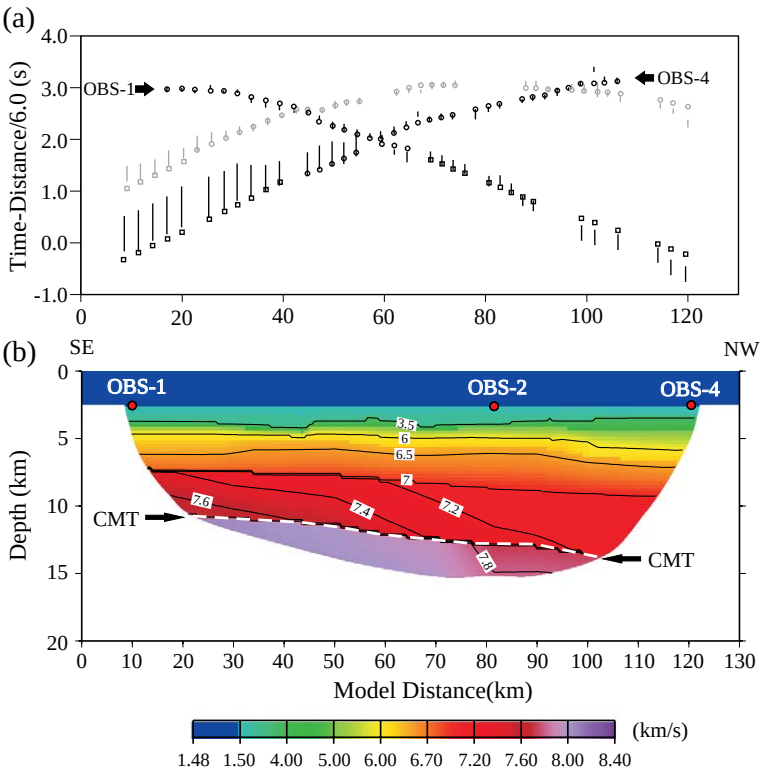

Fig. 7. (a) Observed first-arrivals from OBSs-1,-2 and -4 explosive source record sections (Figs. 3, 4a, 5b) and those calculated from the 2-D model shown in Fig. 7b. Data for OBS-2 is plotted in grey. Each observed pick is plotted as a vertical bar for which the length defines the uncertainty. Calculated Pc arrivals (circles) are differentiated from calculated Pn arrivals (squares). (b) The final velocity model produced from ray tracing and synthetic seismogram analysis. Velocity contours are in km/s. The dashed white line represents the inferred position of the crust–mantle transition (CMT). The region of the model with zero raypath coverage is masked out. Vertical exaggeration is 2.5 : 1.

resides at a greater depth beneath OBS-4 than it does for OBS-1.

The velocity model that best conforms to first arrival, secondary phase, and amplitude observations is shown in Fig. 7b. This model is constructed to satisfy our observations and to show the least amount of deviation from the interpretation of normal oceanic crust by White et al. (1992). The model displays little lateral variation in velocity down to 7 km depth. Below 7 km depth, velocity contours indicate a significant horizontal velocity gradient decreasing to the northwest. Thickened crust in the 2-D velocity model is manifest by velocities representative of crustal material (3.5–7.6 km/s) extending to a greater depth at the northwestern end of the profile than at the southeastern end. The change in sub-sediment crustal thickness, from ~7 km at the southeastern end to ~10 km at the northwestern end, is modelled by collectively enlarging seismic layers 3A and 3B across the profile. This was considered the most appropriate way to model the travel time data because trends identified from the Pc phase could not be attributed to the individual layers of the lower crust.

A reflection Moho phase (PmP) was not identified from the seismic data. The synthetic seismic sections (Figs. 4b, 5c) show that PmP combines with the Pn phase to generate prominent amplitudes and an extended waveform. Consequently, the crust–mantle transition (CMT) is resolved from turning ray phases only and a simple geometry is assumed (Fig. 7b). The upper mantle is modelled with P-wave velocities as low as 7.72 km/s at the northwestern end of the profile in order to limit the thickness of igneous crust to 10 km and still satisfy first arrival travel time observations from greater than 50 km offset on OBS-2 and OBS-4 (Fig. 7a). The anomalous structure is consid-

ered to be well resolved given the high density of data in the center of the line (Figs. 4c, 5d).

Synthetic data generated from the final model confirm the presence of velocity gradients normally associated with igneous crust extending to greater depth at the northwestern end of the model than at the southeastern end. In the model, zones of high velocity gradient bend rays more sharply and focus more energy back to the surface than zones of low velocity gradient. An abrupt decrease in the size of observed first arrival amplitudes with offset should coincide with an abrupt decrease in velocity gradient with depth. This transition takes place at ~60 km offset for both the observed and synthetic receiver gathers for the vertical component of OBS-1 (Fig. 4b). For OBS-4 the transition appears to take place at ~80 km offset (Fig. 5c).

4. Implications of thick crust

The velocity model (Fig. 7b) constructed from all of the available seismic data suggests a dramatic increase in the thickness of the igneous section of oceanic crust, from ~7 to ~10 km directed southeast to northwest. This interpretation implies a crustal thickness increase of 43%. The interpreted 3 km of excess crust should appear as a negative anomaly in the gravity field over the VISP II profile. The free-air gravity field for the northern Juan de Fuca plate is shown in Fig. 8. Some of the features observed in the gravity field can be attributed to topographic features on the oceanic plates and known structural features of the Cascadia subduction zone. These include the broad gravity low centred over the North American continental slope which correlates with the wedge of accretionary wedge sediments interpreted from structural studies across the Cascadia subduction zone (Clowes et al., 1997). The VISP II profile trends parallel to the general regional gradient of the gravity field over the Juan de Fuca plate. Variations in the density structure beneath the seismic line show up as undulations in the gravity field in the direction of the profile (Fig. 9). The negative undulations exhibit wavelengths of ~20 km and a maximum amplitude of 10 mGal. In contrast, the excess crust interpreted

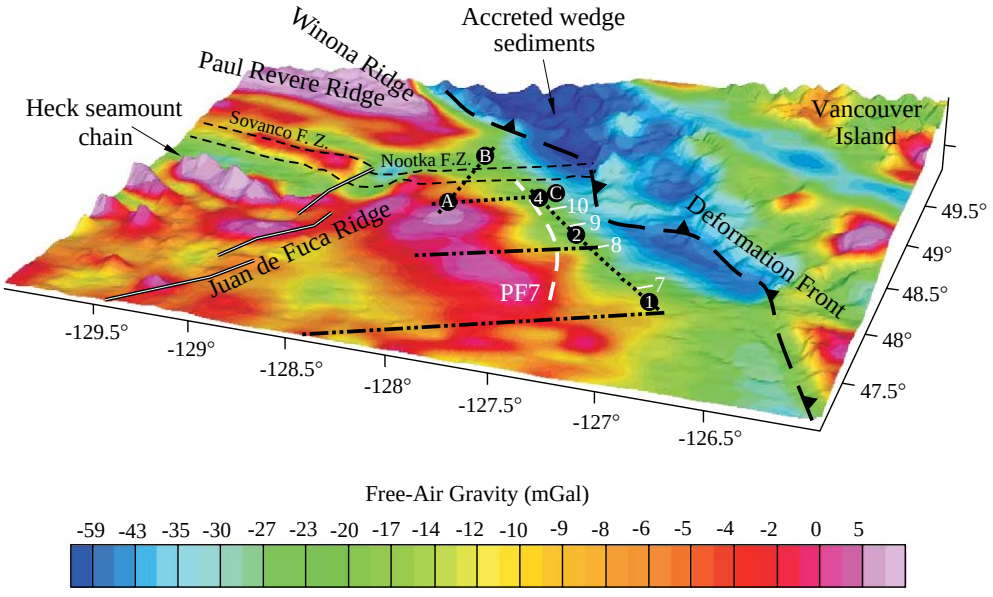

Fig. 8. 3-D perspective of offshore British Columbia: free-air (offshore) and Bouguer (onland) gravity draped over bathymetry and topography. Gravity data are from the 2 km gravity grid from the National Gravity Data Base, maintained by the Geophysical Data Centre of the Geological Survey of Canada. The offshore data are accurate to ± 2 mGal. The prominent bathymetric highs west of the Cascadia deformation front coincide with positive gravity anomalies. Refer to Fig. 1b for identification of seismic lines EX2, EX3, 85-07, 85-09 and VISP II. The dashed white line indicates the trace of pseudofault 7 (PF7). White line annotations along the VISP II profile indicate the thickness in kilometres of the igneous section of oceanic crust as interpreted from the velocity model in Fig. 7.

from Fig. 7 has a horizontal dimension (~70 km) greater than the wavelengths of the negative anomalies along the VISP II profile.

In addition to gravity considerations, anomalously thick oceanic crust is conventionally associated with the influence of a mantle plume. Mantle plumes rising beneath spreading centres supply extra quantities of melt to the crust because they induce additional decompression melting at shallow levels beneath the ridge while seafloor spreading continues (White et al., 1992). For example, the coalescence of the Cobb hotspot with the Juan de Fuca Ridge has resulted in the formation of anomalously thick crust south of the region of this study (West et al., 2003). The interaction of the Cobb hotspot with the spreading ridge has also left behind a pattern of elevated basement topography on the Pacific Plate in the form of the Cobb–Eickelberg seamount chain (West et al., 2003). Variations in basement topography should also be evident from free-air gravity (e.g., the positive gravity anomaly over the Heck seamount chain, Fig. 8). If a mantle plume is responsible for the thick crust interpreted from the VISP II velocity model, it should also influence the elevation of the basement topography. From analysis of the CSP data and the free-air gravity field, we find no evidence for a

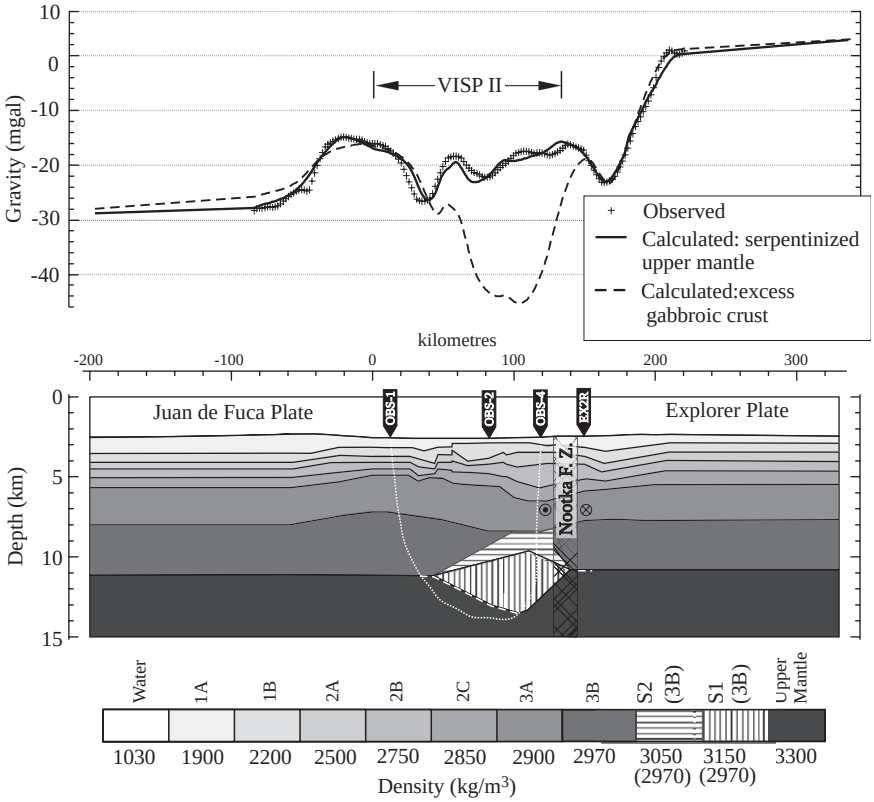

Fig. 9. Two density models along VISP II and its extension (lower panel) and their calculated responses compared to observed free-air gravity (upper panel). The two calculations use differing densities for bodies S1 and S2 (striped areas in lower panel). The solid black line is the calculated gravity for 2 bodies of partially serpentinized upper mantle where S1 represents peridotites containing 25% serpentine by volume and S2 represents peridotites containing 30% serpentine by volume. The dashed black line is calculated gravity for a model of excess gabbroic crust where a density equivalent to layer 3B is used for bodies S1 and S2. The dotted white line bounds the region of the density model constrained by ray tracing through the velocity model. The dashed white line indicates where the CMT is inferred from the VISP II velocity model and a 1-D velocity model on Explorer Plate from refraction line EX2R (Au and Clowes, 1982). Sense symbols indicate the relative motion across the Nootka fault zone. Vertical exaggeration is 12 : 1.

change in basement topography coinciding with the increase in crustal thickness interpreted from the velocity model.

5. Serpentinized upper mantle vs. excess gabbroic crust

In order to explore the nature of the velocity variations at ~10 km depth (excess gabbroic crust versus altered upper mantle), we use our velocity model to place constraints on the density structure by modeling the observed gravity anomaly. The 2-D compressional wave velocity model in Fig. 7b is converted to a 2-D density model using empirically derived velocity/density relationships for marine sediments and normal oceanic crust (Fig. 9). Densities used to describe the 2 sedimentary layers are extracted from Hamilton's (1978) velocity/density relationships for turbidites and mudstone seafloor sediments. Carlson and Raskin (1984) determined a velocity/density relationship from measurements of igneous rocks that compose typical oceanic crust. Density values were determined from this relationship using the average P-wave velocity of seismic layers 2A, 2B, 2C, 3A and 3B established from the velocity model. A value of 3300 kg/m^3 is assigned to the upper mantle consistent with the results of Clowes et al. (1997) from gravity modelling of crustal structure across the Cascadia subduction zone. Each layer of the density model is assumed to extend to infinity normal to the 2-D plane. To reduce edge effects, layers extend an additional 300 km from either end of profile VISP II. Observed gravity values are sampled at 2 km intervals along the extended VISP II line from the gravity grid shown in Fig. 8. Calculated gravity values are obtained from the *SAKI* 2.5-D gravity modelling algorithm (Webring, 1985).

The gravity response of the density model with excess gabbroic crust exhibits a large ~25 mGal low with wavelength of ~100 km, which is clearly discordant with the observed data (Fig. 9). Additional calculations were made to evaluate the effects of limiting the dimensions of the excess crust normal to the profile plane but the revised dimensions did not significantly reduce the wavelength or amplitude of the anomaly. This result discounts our original interpretation of thick crust from the velocity model and indicates the presence of material exhibiting anomalous physical properties at depths equivalent to the lower crust and upper mantle.

Christensen's (1966, 1972) experimental results on ultramafic rocks show that partially serpentinized peridotites are characterized by P-wave velocities equivalent to those of lower crustal gabbroic rocks but they also exhibit a significantly greater rock density (Fig. 10). Fig. 10 illustrates the results obtained at 4 kbar (equivalent to ~12 km depth) and shows Christensen's (1972) interpretation that P-wave velocities (v_p) decrease in a linear fashion with the increasing extent of serpentinization. Note that peridotites consisting of 25% serpentine exhibit a P-wave velocity of 7.2 ± 0.2 km/s and a density of 3100 ± 50 kg/m^3.

Following the empirical relationship shown in Fig. 10, two new density bodies are incorporated into layer 3B of the gravity model to represent a 100 km long zone of partially serpentinized upper mantle (Fig. 9). Body S1 (3150 kg/m^3) is used to model the region of seismic layer 3B that exhibits v_p velocities of 7.2 ± 0.05 km/s and body S2 (3050 kg/m^3) for v_p velocities of 7.1 ± 0.05 km/s (Figs. 7b, 9, 10). Bodies S1 and S2 represent peridotite rocks containing 25% and 30% serpentine by volume, respectively. The corresponding P-wave velocities and densities lie within 1 standard deviation of those measured in Fig. 10. The calculated response is shown in Fig. 9. Minor adjustments were made to the geometries of layers 1A, 1B, 2C, 3A and 3B to reduce the root-mean-square (RMS) of the gravity residuals to 1.87 mGal, values within measurement uncertainty.

The same changes to the density model layer boundaries are applied to the velocity model to evaluate the new misfit to the picked first arrival phases. The statistics of the first arrival misfit from ray tracing through the velocity model before and after the adaptation are displayed in Table 5. The modifications have increased the misfit but not to an unsatisfactory extent. Of all the measurements used to integrate the 2 models, those used to define the velocity–density relationships carry the greatest uncertainty. For example, Christensen's (1996) measurements of 252 basalt specimens at 2 kbar (equivalent to ~6 km depth) exhibit standard deviations for P-wave velocity and density of 0.546 km/s and 139 kg/m^3 respectively. Perturbing just layer 2A

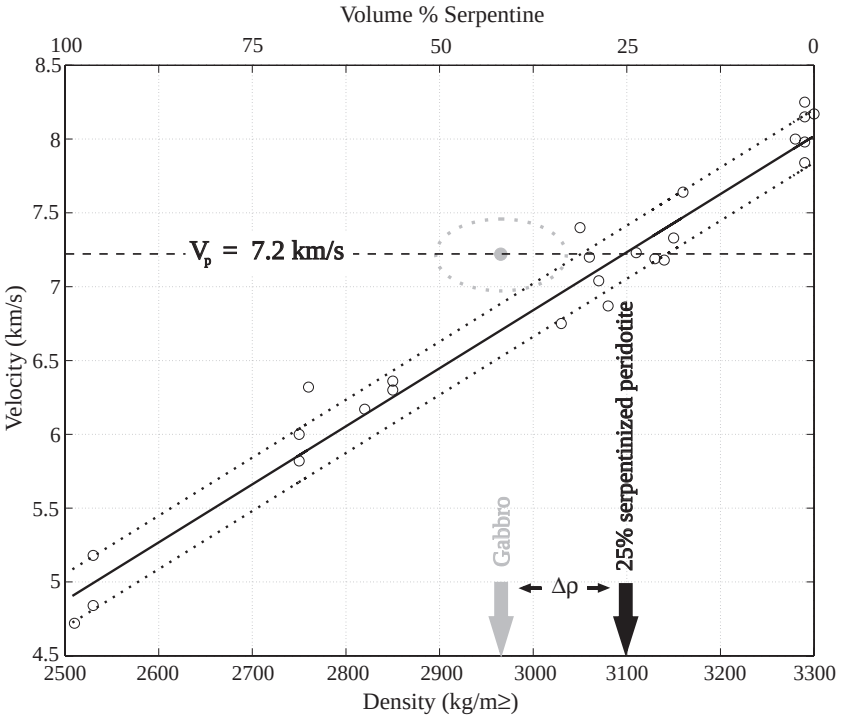

Fig. 10. P-wave velocities at 4 kbar versus density and volume percent serpentine for peridotites and serpentinized peridotites (open circles). The solid line represents the least squares fit and the dotted lines represent the standard deviation of the residuals from the measurements of Christensen (1966). The mean value (solid circle) and standard deviation (dotted ellipse) for a suite of gabbro samples from Christensen (1996) also are shown. $\Delta\rho$ indicates the contrast in density at 7.2 km/s for gabbros and peridotites containing 25% serpentine.

of the velocity model by 0.5 km/s yields a calculated χ^2 misfit of 2.218. Therefore, the difference in misfit between the best-fit velocity model and the velocity model modified to reconcile with the density model is within acceptable error.

6. Additional evidence for anomalous crustal structure near VISP II

Two independent seismic experiments in the immediate vicinity of the VISP II profile provide complementary evidence for unusual velocity structure and crustal characteristics within northern Juan de Fuca plate (seismic lines EX2, EX3 and 85-07, Fig. 1b). The unusual travel time delays observed from the VISP II receiver gathers, which yield the model of upper mantle serpentinization (Fig. 9), are replicated by refraction data from an earlier experiment over the Nootka fault zone (Au and Clowes, 1982). Refraction line EX3 is oriented parallel and to the south of the Nootka fault zone (Fig. 1b). 1-D velocity models constructed to fit travel time and amplitude observations from forward and reversed sections of line EX3 indicate an igneous crustal thickness of ~10 km. This is in contrast to 1-D models constructed from observations from line EX2, which traverses the Nootka fault zone with a north–south orientation (Fig. 1b). Au and Clowes' (1982) interpretation of the velocity models suggests an igneous crustal thick-

Table 5
T_{RMS} and χ^2 of first arrival residual travel times for the 2-D velocity model before and after reconciliation with the density model illustrated in Fig. 9

	Before	After
T_{RMS} (s)	0.137	0.143
χ^2	1.604	2.229
n	189	189

ness of between 6 and 8 km. Collectively, the 1-D models imply an anomalous low velocity zone at depths between 9 and 13 km that is confined to the Juan de Fuca plate.

In 1985, a number of multichannel seismic reflection (MCS) lines were recorded off the west coast of British Columbia for the purpose of investigating the lithospheric structure over the continental margin and adjacent Juan de Fuca plate. Hasselgren and Clowes (1995) present the results from lines 85-07 and 85-09 which trend perpendicular to and southwest of the VISP II profile (Fig. 1b). They observe continuous, coherent reflection Moho at 6–6.5 s two-way travel time (TWT) on both lines 85-07 and 85-09 (Fig. 11a,c). By assuming an average velocity through the crust of 6000 m/s, the depth calculated for the top of the crust–mantle transition (CMT) reflector varies as little as 600 m for most of the length of each profile. However, at the eastern end of line 85-07 (shot points 1–600 in Fig. 11a) CMT reflectors disappear and are replaced by an anomalous zone extending from 5 s to at least 7 s TWT containing dipping, discontinuous reflectors. The abrupt change in the pattern of reflectivity occurs at the intersection of line 85-07 with pseudofault 7 (Figs. 1b, 11a and b) suggesting a relationship between the two (Hasselgren et al., 1992). Interval velocities derived from stacking velocities for the deep reflectors indicate velocities of the range 6.6–7.5 km/s, typical of lower crustal gabbroic material. Hasselgren et al. (1992) first speculated that the complex reflectivity results from the inter-layering of materials with contrasting mafic content within anomalously thick lower crust. Alternatively, based on our results from VISP II and the gravity modelling, the unusual zone may coincide with discrete zones of extensively serpentinized peridotite within the upper mantle. Calvert et al. (1990) observed a similar pattern of reflectivity where pseudofault 4 crosses line 85-09 (Figs. 1b, 11c and d).

The discrimination between excess gabbroic crust and serpentinized upper mantle for profiles EX3 and 85-07 requires an analysis of the local gravity field. Unlike seismic line VISP II, profiles EX3 and 85-07 are oriented perpendicular to the structural grain of the Cascadia subduction zone. Consequently, at these orientations, variations in the gravity field resulting from local structure are overprinted with the regional variation of larger scale structure attributable to the adjacent subduction zone (Fig. 8). For example, accretionary wedge sediments east of the deformation front and the deepening of the lithosphere as it subducts beneath North America contribute to the large negative gravity gradient in a northeasterly direction toward the continental rise.

The gravitational effects of the Cascadia subduction zone make it difficult to discriminate a gravity low expected from the onset of thick crust along seismic lines EX3 and 85-07 (Fig. 8). Nevertheless, the 2-D gravity model produced to represent excess crust, as originally interpreted from the VISP II velocity model, demonstrates that a 3 km increase in crustal thickness results in a prominent negative gravity anomaly with large amplitude (~25 mGal, Fig. 9) that does not feature in the free-air gravity field displayed in Fig. 8. Au and Clowes' (1982) 1-D velocity models across the Nootka fault zone indicate that crustal thickness changes from 6–8 km beneath line EX2 to ~10 km beneath line EX3. An increase in crustal thickness of 2–4 km between lines EX2 and EX3 should produce a gravity anomaly comparable to that predicted along line VISP II (Fig. 9). Aside from regional variations in the gravity field that are apparent along both lines EX2 and EX3, we find no evidence for a negative gravity anomaly attributable to excess crust. The same argument can be used to refute the presence of thick crust beneath the eastern end of seismic line 85-07.

7. Discussion

Based on proximity to the VISP II profile and an analysis of the gravity data, we infer that the low velocity zone observed from refraction line EX3 and the zone of unusual reflectivity recorded on line 85-07 are associated with serpentinized upper mantle. In combination with results along the VISP II profile, we thus postulate the existence of a broad zone of partially serpentinized upper mantle peridotite that coincides with 2–6 Ma lithosphere formed astride pseudofault 7 (Fig. 12).

The most significant change in composition induced by the serpentinization of peridotite is the addition of up to 15 weight % H_2O (O'Hanley, 1996). Large volumes of water are required both to

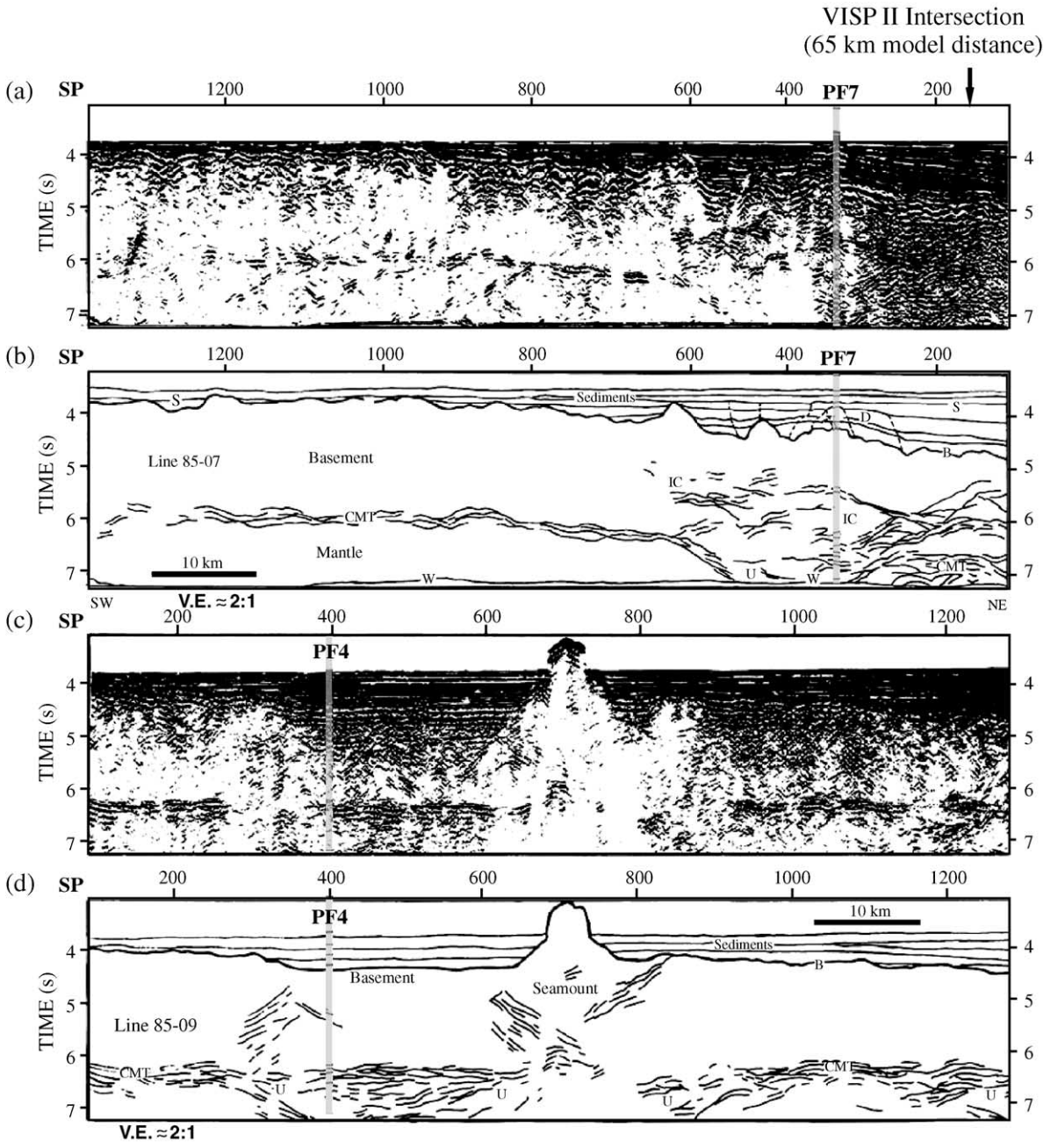

Fig. 11. (a) Coherency-filtered stack of line 85-07. (b) Line drawing of interpreted primary reflections of line 85-07. (c) Coherency-filtered stack of the southwestern end of line 85-09. (d) Line drawing of interpreted primary reflections for 85-09. S is sediments; D is disrupted sediments; B is top of igneous crust; W is water bottom multiple. Hasselgren and Clowes (1995) interpreted IC as intracrustal reflectors and U as an underplated zone. The intersection of pseudofault traces 4 and 7 (Fig. 1b) are indicated with grey lines. Note that in each case, they correspond to regions of anomalous reflectivity. Reproduced from Hasselgren and Clowes (1995).

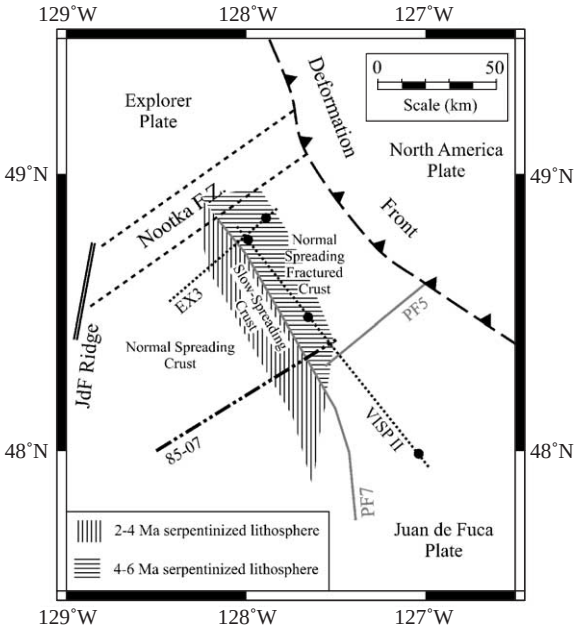

Fig. 12. Conceptual model for serpentinization of northern Juan de Fuca lithospheric mantle. See text for discussion.

form serpentine minerals from existing ultramafic minerals and to remove elements not found in the serpentine product. In addition, temperatures must be less than about 500 °C for the serpentinization process to become stable (O'Hanley, 1996). At distances close to the axial regions of mid-ocean ridges, hydrothermal circulation of seawater contributes a high flux of seawater through the upper crust that can potentially permeate to upper mantle depths. In addition, hydrothermal circulation can convectively cool the recently created lithosphere such that temperatures within the upper mantle can fall below 500 °C within a short distance from the spreading ridge axis, allowing favourable conditions for serpentine formation (Francis, 1981). The maintenance of a high flow rate of seawater penetration into the upper mantle requires permeable pathways like faults or fractures.

Fryer (2002) and O'Hanley (1996) describe a process of oceanic crustal formation and modification that may explain why serpentinized peridotites are frequently recovered from fault escarpments within slow-spreading (1 to 5 cm/yr) ridge axes such as the Mid-Atlantic Ridge and not from fast-spreading (greater than 9 cm) ridge axes like the East Pacific Rise. Unlike fast-spreading ridges, the supply of magma to slow-spreading ridges is episodic, suggesting that the ridge will endure amagmatic periods. The crust will thin without the addition of new magma to the spreading plates and does so by normal faulting (White et al., 1990; Salisbury and Keen, 1993). In addition, the absent heat source beneath a ridge during a period of amagmatism allows isotherms to deepen such that temperatures within the mantle are conducive to serpentinization. The normal faults provide the necessary pathways for seawater penetration into the upper mantle.

Segments of the Juan de Fuca ridge system have spread at average rates of anywhere between 4 and 6 cm/yr since 6 Ma (Riddihough and Hyndman, 1991). Favourable conditions for upper mantle serpentinization may have occurred at the ends of propagating rift segments where the melt supply to the ridge tip is reduced (Hey et al., 1980). At the Galapagos 95.5°W propagator, ~21 km of irregular rift tip spreading precedes normal spreading at the trailing ridge axis (Kleinrock and Hey, 1989). Pseudofault 7 is an outer pseudofault that according to conceptual models for the development of pseudofault zones (Hey et al., 1980; Kleinrock and Hey, 1989) should record a zone of transitional rifting along the inboard margin of the pseudofault trace. From a combined wide-angle seismic and gravity study, Canales et al. (2000) infer a zone of partial serpentinization extending from depths of 3.8 to 6.2 km beneath crust at a nontransform offset of the Mid-Atlantic Ridge. If the slow-spreading crust formed near outer pseudofaults exhibits similar crustal accretion characteristics as slow-spreading crust formed at nontransform offsets, it follows that the upper mantle near a pseudofault may be equally susceptible to serpentine formation.

From seismic lines EX3 and 85-07, we interpret a zone of serpentinization about 20 km wide and 100 km long beneath 2–4 Ma crust coincident with the predicted outer pseudofault zone west of PF7 (Fig. 12). The hydration of an ~20 km wide and ~80 km long zone of adjacent lithosphere aged 4 to 6 Ma, corresponding to the low velocity zone observed from line VISP II, may have occurred over the same time interval (2–4 Ma). Upper mantle juxtaposed against newly created lithosphere will have undergone 2 mil-

lion years of cooling by the time the propagating ridge passed along the trace of PF7. Consequently, temperatures within the upper mantle of the older lithosphere would have been favourable for serpentine formation. In addition, upper mantle proximal to the trace of PF7 would have been susceptible to percolating waters emanating from the propagating ridge as it migrated northward. Initial separation of the Explorer plate from the Juan de Fuca plate occurred at ~4 Ma, prior to the time the rift was propagating through this area. Either a diffuse plate boundary, or the migration of the Nootka fault system northward to its present location, deformed the 4–6 Ma crust east of PF7 (Wilson, 1993). Fracturing associated with this deformation may have provided additional pathways for circulating seawater to penetrate the upper mantle at distances up to 20 km from the spreading ridge as it passed. Propagating rift 7 had reached the present-day position of the Nootka fault zone by 1.5 Ma. Active deformation within a wide fault zone would have provided numerous pathways for seawater to penetrate the upper mantle at this time. This may explain why the greatest thickness of serpentinized peridotite, inferred from the velocity model of VISP II, occurs close to the present-day position of the Nootka fault zone (Fig. 9).

The zone of serpentinization interpreted at the intersection of reflection line 85-09 with pseudofault 4 exhibits a similar pattern of discrete dipping reflectors as that observed on line 85-07 at the intersection with PF7 (Fig. 11c,a). We suggest that serpentinization of the upper mantle took place in a similar manner at both locations.

Hydration and serpentinization of lithospheric mantle may be a common feature at pseudofaults. The serpentinization regime inferred in this study is analogous to that described by Canales et al. (2000) from their interpretation of a combined wide-angle seismic and gravity study over a nontransform offset of the slow spreading Mid-Atlantic Ridge. Kruse et al. (2000) found that gravity anomalies over pseudofaults in medium to superfast spreading environments are similar in amplitude and form to those over fracture zones at the slow spreading Mid-Atlantic Ridge, suggesting similarities in crustal structure. Future studies of oceanic lithosphere formed at pseudofaults that integrate high resolution seismic and gravity data may confirm whether serpentinization is a common process associated with propagating rift events.

Ranero et al. (2003) show convincing evidence for bending-related faulting at the Middle America trench and implicate these structures as conduits for hydration of the cold crust and upper mantle. Serpentinization of the oceanic upper mantle by bending-related faulting is predicted to become significant within 25 km of the trench axis, reaching a maximum of 30% serpentinization at Moho depths closest to the trench. This serpentinized mantle potentially contributes as much chemically bound water to the subducting slab as does the oceanic crust. If bending-related faulting is a common process along subduction zones worldwide, then serpentinization of the underlying oceanic upper mantle represents a significant contribution to the slab fluid budget which has implications for slab recycling and arc magmatism (Ranero et al., 2003). The serpentinization of oceanic upper mantle by propagation rifting may contribute additional slab fluids prior to bending at a subduction trench. Alternatively, localized hydration of oceanic upper mantle around pseudofaults may become overprinted by subsequent along-axis hydration of the oceanic lithosphere beneath bending-related deformation as the slab approaches the subduction trench.

8. Conclusions

Two-dimensional forward and inverse modelling of seismic refraction data reveals the presence of anomalously low velocities within northern Juan de Fuca plate. The zone of low velocities is modelled beneath the VISP II profile to extend for approximately 100 km and resides at depths typically associated with seismic layer 3B and the upper mantle of normal oceanic lithosphere. Synthetic seismograms generated for first arrival phases from the model are in good agreement with the recorded sections and confirm the existence of a lateral velocity gradient at sub-sediment depths of ~3 to ~10 km. The best-fit velocity model suggests that sub-sediment oceanic crust increases in thickness from ~7 to ~10 km from southeast to northwest (a thickness increase of 43%).

A two-dimensional density model, constructed from the conversion of P-wave velocities using

standard velocity–density relationships for oceanic crust, produces a large (25 mGal) gravity low with a wavelength of ~140 km that is not evident in the free-air gravity anomaly. The incorporation of gravity data discounts the thick crust hypothesis and indicates the existence of a zone of upper mantle peridotites containing 25–30% serpentine by volume. The modelled zone of partially serpentinized peridotite has P-wave velocities of 7–7.2 km/s and densities of 3050–3150 kg/m^3. Exclusive of this region, seismic refraction and gravity modelling reveal seismic velocities and densities typical of normal oceanic crust.

Interpretations from proximal seismic refraction and reflection lines EX2, EX3 (Au and Clowes, 1982) and 85-07 (Hasselgren and Clowes, 1995) confirm the existence of unusual crustal and upper mantle structure near VISP II and imply that the region of serpentinized upper mantle coincides with a 40 km wide zone of 2–6 Ma crust on either side of a pseudofault trace that terminates at the Nootka fault zone.

We suggest that the process of serpentinization resulted from a northward propagating rift that juxtaposed lithosphere with a 2 million year age contrast. Slow rates of accretion at the propagating rift tip between 2–4 Ma were conducive to lithosphere hydration and subsequent serpentinization, which occurred over a zone on the inboard side of the trailing outer pseudofault. Upper mantle temperatures within older lithosphere on the outboard side of the pseudofault cooled to within the serpentine stability field at the time of rifting. The formation of the Nootka fault zone pervasively fractured 4–6 Ma aged crust on the outboard side of the propagating rift tip allowing hydrothermal currents that emanated at the propagating rift to efficiently percolate through the crust and serpentinize the underlying upper mantle.

Acknowledgements

We would like to acknowledge the important contributions of the late Hugh R.W. White, who carried out a preliminary analysis of VISP II data and left the hard copy seismograms on which this study is based. Financial support was provided through a Science and Engineering Research Canada (NSERC) Discovery grant to R. M. Clowes.

References

Au, D., Clowes, R.M., 1982. Crustal structure from an OBS survey of the Nootka fault zone off western Canada. Geophys. J. R. Astron. Soc. 68, 27–47.

Best, A.I., Huggett, Q.J., Harris, J.K., 2001. Comparison of in situ and laboratory acoustic measurements on Lough Hyne marine sediments. J. Acoust. Soc. Am. 110, 695–709.

Calvert, A.J., Hasselgren, E.O., Clowes, R.M., 1990. Oceanic rift propagation — a cause of crustal underplating and seamount volcanism. Geology 18, 886–889.

Canales, J.P., Detrick, R.S., Lin, J., Collins, J.A., 2000. Crustal and upper mantle seismic structure beneath the rift mountains and across a nontransform offset at the Mid-Atlantic Ridge (35°N). J. Geophys. Res. 105, 2699–2719.

Carlson, R.L., Raskin, G.S., 1984. Density of the ocean crust. Nature 311, 555–558.

Christensen, N.I., 1966. Elasticity of ultrabasic rocks. J. Geophys. Res. 71, 5921–5931.

Christensen, N.I., 1972. The abundance of serpentinites in the oceanic crust. J. Geol. 80, 709–719.

Christensen, N.I., 1978. Ophiolites, seismic velocities and oceanic crustal structure. Tectonophysics 47, 131–157.

Christensen, N.I., 1996. Poisson's ratio and crustal seismology. J. Geophys. Res. 101, 3139–3156.

Clowes, R.M., Baird, D.J., Dehler, S.A., 1997. Crustal structure of the Cascadia subduction zone, southwestern British Columbia, from potential field and seismic studies. Can. J. Earth Sci. 34, 317–335.

Davis, E.E., Currie, R.G., 1993. Geophysical observations of the northern Juan de Fuca Ridge system: lessons in sea-floor spreading. Can. J. Earth Sci. 30, 278–300.

Detrick, R.S., White, R.S., Purdy, G.M., 1993. Crustal structure of North Atlantic fracture zones. Rev. Geophys. 31, 439–458.

Ellis, R.M., Spence, G.D., Clowes, R.M., Waldron, D.A., Jones, I.F., Green, A.G., Forsyth, D.A., Mair, J.A., Berry, M.J., Mereu, R.F., Kanasewich, E.R., Cumming, G.L., Hajnal, Z., Hyndman, R.D., McMechan, G.A., Loncarevic, B.D., 1983. The Vancouver Island Seismic Project: a CO-CRUST onshore–offshore study of a convergent margin. Can. J. Earth Sci. 20, 719–741.

Ewing, J., Houtz, R., 1979. Acoustic stratigraphy and structure of the oceanic crust. In: Talwani, M., Harrison, C.G.A., Hayes, D.E. (Eds.), Deep Drilling Results in the Atlantic Ocean. American Geophysical Union, pp. 1–14.

Fox, P.J., Gallo, D.G., 1984. A tectonic model for ridge-transform–ridge plate boundaries. Tectonophysics 104, 205–242.

Francis, T.J.G., 1981. Serpentinization faults and their role in the tectonics of slow spreading ridges. J. Geophys. Res. 86, 11616–11622.

Fryer, P., 2002. Recent studies of serpentinite occurrences in the oceans: mantle–ocean interactions in the plate tectonic cycle. Chemie der Erde-Geochemistry 62, 257–302.

Hamilton, E.L., 1978. Sound velocity–density relations in seafloor sediments and rocks. J. Acoust. Soc. Am. 63, 366–377.

Hasselgren, E.O., Clowes, R.M., 1995. Crustal structure of northern Juan de Fuca plate from multichannel reflection data. J. Geophys. Res. 100, 6469–6486.

Hasselgren, E.O., Clowes, R.M., Calvert, A.J., 1992. Propagating rift pseudofaults — zones of crustal underplating imaged by multichannel seismic reflection data. Geophys. Res. Lett. 19, 485–488.

Hey, R., Duennebier, F.K., Morgan, W.J., 1980. Propagating rifts on midocean ridges. J. Geophys. Res. 85, 3647–3658.

Jacobson, R.S., Lewis, B.T.R., 1990. The first direct measurements of upper oceanic crustal compressional wave attenuation. J. Geophys. Res. 95, 17417–17429.

Kleinrock, M.C., Hey, R.N., 1989. Detailed tectonics near the Galapagos 95.5°W propagator: how the lithosphere tears and a spreading axis develops. J. Geophys. Res. 94 (13), 13801–13838.

Kruse, S.E., Tebbens, S.F., Naar, D.F., Lou, Q., Bird, R.T., 2000. Comparisons of gravity anomalies at pseudofaults, fracture zones, and nontransform discontinuities from fast to slow spreading areas. J. Geophys. Res. 105, 28399–28410.

Mueller, St., Stein, A., Veis, R., 1962. Seismic scaling laws for explosions on a lake bottom. Z. Geophys. 28, 258–280.

O'Brien, P.N.S., 1960. Seismic energy from explosions. Geophys. J. R. Astron. Soc. 3, 29–44.

O'Hanley, D.S., 1996. Serpentinites: records of tectonic and petrological history. Oxf. Monogr. Geol. Geophys. 34 (277 pp.).

Ranero, C.R., Phipps Morgan, J., McIntosh, K., Reichert, C., 2003. Bending-related faulting and mantle serpentinization at the Middle America trench. Nature 425, 367–373.

Riddihough, R.P., Hyndman, R.D., 1991. Modern plate tectonic regime of the continental margin of western Canada. In: Gabrielse, H., Yorath, C.J. (Eds.), Geology of the Cordilleran Orogen in Canada, Geological Survey of Canada, Geology of Canada, vol. 4, pp. 435–455.

Salisbury, M.H., Keen, C.E., 1993. Listric faults imaged in oceanic crust. Geology 21, 117–120.

Spudich, P., Orcutt, J., 1980. Petrology and porosity of an oceanic crustal site: results from waveform modeling of seismic refraction data. J. Geophys. Res. 85, 1409–1433.

Webring M., 1985. SAKI: a fortran program for generalized linear inversion of gravity and magnetic profiles. Open file report. United States Department of the Interior, Geological Survey. 85-122.

West, M., Menke, W., Tolstoy, M., 2003. Focused magma supply at the intersection of the Cobb hotspot and the Juan de Fuca ridge. Geophys. Res. Lett. 30, 1724, doi:10.1029/2003GL017104.

White, R.S., Detrick, R.S., Mutter, J.C., Buhl, P., Minshull, T.A., Morris, E., 1990. New seismic images of oceanic crustal structure. Geology 18, 462–465.

White, R.S., McKenzie, D., O'Nions, R.K., 1992. Oceanic crustal thickness from seismic measurements and rare earth element inversions. J. Geophys. Res. 97, 19683–19715.

Wilson, D.S., 1993. Confidence intervals for motion and deformation of the Juan de Fuca plate. J. Geophys. Res. 98, 16053–16071.

Wilson, D.S., Hey, R.N., Nishimura, C., 1984. Propagation as a means of reorientation of the Juan de Fuca ridge. J. Geophys. Res. 89, 9215–9225.

Zelt, C.A., 1999. Modelling strategies and model assessment for wide-angle seismic traveltime data. Geophys. J. Int. 139, 183–204.

Zelt, C.A., Ellis, R.M., 1988. Practical and efficient ray tracing in two-dimensional media for rapid traveltime and amplitude forward modelling. Can. J. Explor. Geophys. 24, 16–31.

Zelt, C.A., Smith, R.B., 1992. Seismic traveltime inversion for 2-D crustal velocity structure. Geophys. J. Int. 108, 16–34.